Cellulose (2013) 20:2703–2718
DOI 10.1007/s10570-013-0071-8

ORIGINAL PAPER

Anisotropy of the elastic properties of crystalline cellulose I_β from first principles density functional theory with Van der Waals interactions

Fernando L. Dri · Louis G. Hector Jr. · Robert J. Moon · Pablo D. Zavattieri

Received: 28 July 2013 / Accepted: 26 September 2013 / Published online: 10 October 2013

Abstract In spite of the significant potential of cellulose nanocrystals as functional nanoparticles for numerous applications, a fundamental understanding of the mechanical properties of defect-free, crystalline cellulose is still lacking. In this paper, the elasticity matrix for cellulose I_β with hydrogen bonding network A was calculated using ab initio density functional theory with a semi-empirical correction for van der Waals interactions. The computed Young's modulus is found to be 206 GPa along [001] (*c*-axis), 98 GPa along [010] (*b*-axis), and 19 GPa along [100] (*a*-axis). Full compliance matrices are reported for 1.0, 1.5 and 2.0 % applied strains Color contour surfaces that show variations of the Young's modulus and average Poisson's ratio with crystallographic direction revealed the extreme anisotropies of these important mechanical properties. The sensitivity of the elastic parameters to misalignments in the crystal were examined with 2D polar plots within selected planes containing specific bonding characteristics; these are used to explain the substantial variability in the reported experimental Young's moduli values. Results for the lattice directions [001], [010] and [100] are within the range of reported experimental and other numerical values.

Keywords Crystalline cellulose · Cellulose Iβ · Density functional theory · Young's modulus

F. L. Dri · P. D. Zavattieri (✉)
School of Civil Engineering, Purdue University, 550 Stadium Mall Drive, West Lafayette, IN 47907-2051, USA
e-mail: zavattie@purdue.edu

L. G. Hector Jr.
Chemical Sciences and Materials Systems Laboratory, General Motors Research and Development Center, Warren, MI 48090, USA

R. J. Moon
School of Materials Engineering and Birck Nanotechnology Center, Purdue University, West Lafayette, IN 47907, USA

R. J. Moon
USDA Forest Service, Forest Products Laboratory, Madison, WI 53726, USA

Introduction

Mechanical properties of cellulose nanocrystals (CNCs) are difficult to experimentally characterize owing largely to extreme anisotropy and uncertainties about the structure of these materials. For example, reported experimental values for the Young modulus of cellulose I_β show a wide variation that is hard to explain considering the defect-free crystalline structure typically observed in CNCs (Sakurada et al. 1962, 1964; Matsuo et al. 1990; Roberts et al. 1994; Nishino et al. 1995; Ishikawa et al. 1997; Diddens et al. 2008; Wagner et al. 2011; Pakzad et al. 2012; Lahiji et al. 2010). Unfortunately, there is no standardization of the coordinate system and nomenclature used to measure

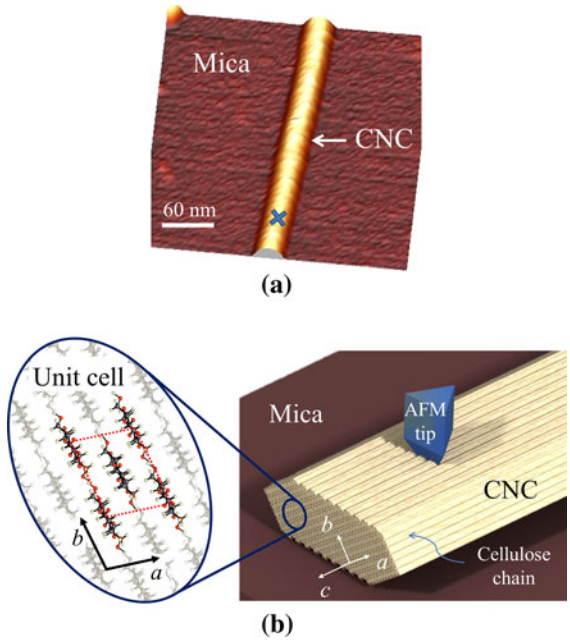

Fig. 1 **a** Atomic force microscope topography image of a tunicate CNC showing its rod-like shape (on a mica substrate) (Wagner et al. 2011). The *blue cross* near the bottom of the figure denotes a location for AFM tip indentation. **b** Schematic of a CNC particle during AFM indentation for illustration purposes. Here, the cellulose chains are represented by *straight ribbons*, and the crystallographic directions indicated as *a*, *b* and *c*. The *inset* shows details of the layered cellulose structure where *red spheres* denote oxygen ions, *gray spheres* represent carbon ions and *white spheres* represent hydrogen ions. The *red dotted lines* indicate the repeating unit cell. (Color figure online)

the elastic moduli making quantitative comparisons of the elastic behavior between experiments and theory rather difficult. Most authors agree on defining both an axial or longitudinal Young modulus, E_A, which is aligned with the longitudinal axis of the cellulose I_β unit cell, and an additional Young modulus, perpendicular to the longitudinal axis, usually reported as the transverse modulus, E_T. Early studies using X-ray diffraction (Sakurada et al. 1962, 1964; Matsuo et al. 1990; Nishino et al. 1995; Ishikawa et al. 1997) measured values of E_A ranging from 90 to 138 GPa. Recently, Diddens et al. (2008) reported values of $E_A = 220 \pm 50$ GPa and $E_T = 15 \pm 1$ GPa using inelastic X-ray scattering (IXS). Diddens et al. (2008) claimed that IXS was not affected by the amorphous zones occurring in natural cellulose, and the elastic behavior was mostly related to the highly crystalline regions. Alternatively, larger uncertainties have been reported from atomic force microscopy (AFM) measurements of cellulose I_β elastic properties. For example, Lahiji et al. (2010) and Wagner et al. (2011) reported $E_T = 8.1$ GPa with a 95 % confidence, which translates into an interval ranging from 2.7 to 20 GPa.

A typical AFM indentation test of a CNC particle on a hard substrate is shown in Fig. 1a. As described by Lahiji et al. (2010), this test is used to measure E_T. Figure 1b shows schematics of the direction of the load with respect to the expected crystallographic directions (*a*, *b* and *c*). Relating these experimental measurements to a specific crystallographic orientation is challenging since it is difficult to estimate the alignment of the CNC with respect to the substrate (Lahiji et al. 2010). Moreover, with no additional information on the direction assigned to E_T, it may not be possible to properly interpret the experimental data and, therefore, any attempt to compare experiments with computational predictions is difficult. Uncertainties about the shape of the CNC after sample preparation and the determination of the crystallographic planes during the experiments contribute to this important challenge.

In the present study, we quantify the anisotropy of the Young's modulus and Poisson's ratio of monoclinic cellulose I_β using ab initio first principles density functional theory (DFT) (Kohn and Sham 1965) with a semi-empirical correction for van der Waals interactions (Bučko et al. 2010). The least squares fitting method of Le Page and Saxe (2002) is used to compute all unique components of the elastic stiffness and compliance matrices using the VASP code (Kresse and Hafner 1994; Kresse and Furthmuller 1996a, b; Hafner 2008) as the DFT computational engine. This information enables analysis of the variations of the Young's modulus and Poisson's ratio with crystallographic orientation. These variations are displayed as surfaces which are color contours showing crystallographic dependence of these properties. Polar plots, which show the Young's modulus and Poisson's ratio variation with angular orientation in a given plane within the cellulose I_β crystal structure, are used to: (1) explain the substantial variability in the literature experimental data of the Young's modulus for cellulose, and (2) understand the Poisson's effect in selected planes.

Background

Cellulose $[[C_6H_{10}O_5]_n$, $n = 10{,}000$–$15{,}000$, where n depends upon the cellulose source material (Azizi

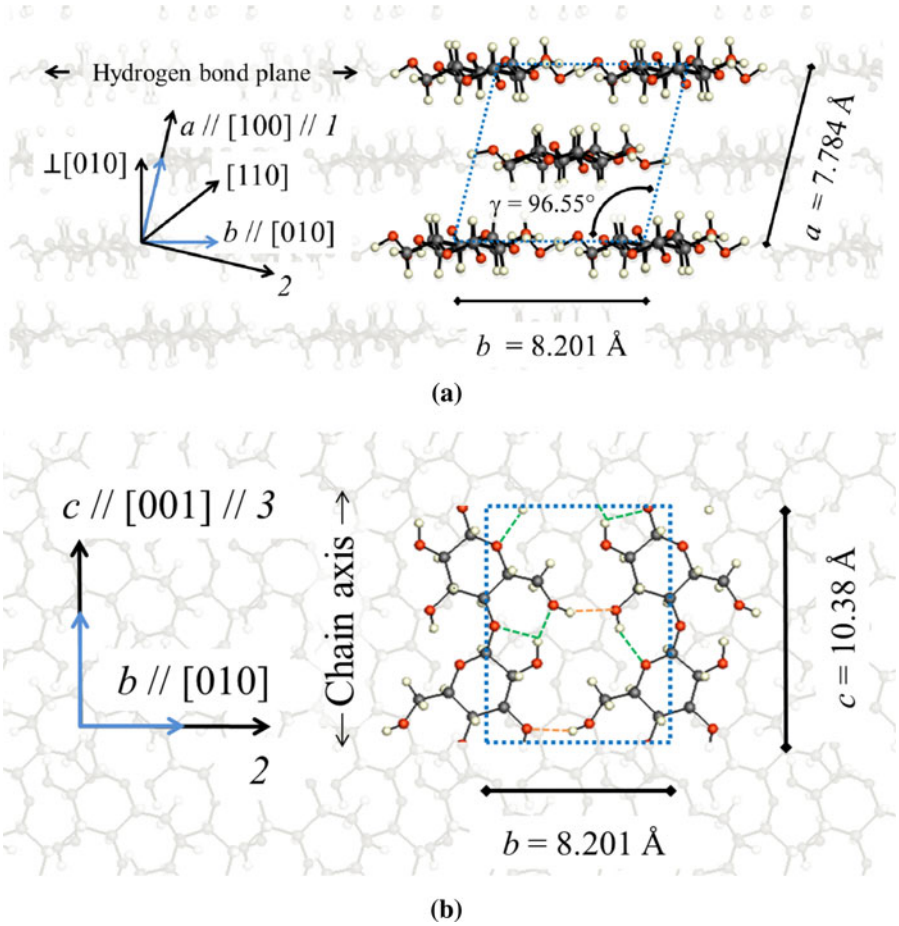

Fig. 2 Expanded views of the $P2_1$ unit cell structure of the cellulose I_β network A showing the characteristic layered conformation (Zuluaga et al. 2013b). Experimental (room temperature) lattice parameters *a*, *b*, *c*, from Nishiyama et al. (2002) are shown. *Red spheres* denote oxygen ions, *gray spheres* represent carbon ions and *white spheres* represent hydrogen ions. *Dotted blue lines* denote the unit cell. **a** View along the *c*-axis (perpendicular to the page). Layers of I_β are stacked along the *a*-axis. **b** View along the *a*-axis direction. Atomic coordinates were obtained after applying symmetry operations to the original structure reported by Nishiyama et al. (2002). Intra- and intermolecular hydrogen bonds are depicted in *green* and *orange* respectively, according to the hydrogen bond network A pattern reported in Refs. Nishiyama et al. (2008) and Šturcová et al. (2004). The symbol // in this figure means "parallel to." For example, *a*//[001]//*1* means that the crystallographic direction *a*, with Miller indices [001], is parallel to the Cartesian axis *1*. (Color figure online)

Samir et al. 2005)] is an organic compound that can be described as a linear chain of glucose rings with a flat ribbon-like conformation. Each chain is formed by one-hundred to over ten-thousand β (1 → 4) linked D-glucose units; van der Waals (vdW) and intermolecular hydrogen bonds promote parallel stacking of multiple cellulose chains within the crystal (Nishiyama et al. 2008; Wada et al. 2008) forming the characteristic layered structure along the *a* crystallographic direction (see Fig. 2a).

The most basic classification method divides crystalline cellulose types into 4 basic polymorphs that are identified as I, II, III or IV, each one having its own subtype (Moon et al. 2011). Cellulose I, also called native cellulose, has a mix of two polymorphs, viz., cellulose I_α, which has a triclinic P_1 (#1) structure, and I_β, which has a monoclinic $P2_1$ (#4) structure, that coexist in various proportions depending on the source of the CNC (Nishiyama et al. 2002, 2003). The I_α structure is the dominant polymorph in most algae and bacteria, whereas I_β is the dominant polymorph for higher plant cell wall cellulose and in tunicates (Parthasarathi et al. 2011; Moon et al. 2011). A further classification of cellulose I can be based on the

hydrogen bond network patterns, A and B, proposed by Nishiyama et al. (2002). The relative occupancies of the two networks are different according to the polymorph: network A occupies ~70–80 % of all the chain positions in I_β, but only ~55 % in I_α (Nishiyama et al. 2003, 2008). This study focuses on cellulose I_β with network A since it is the most commonly occurring polymorph in higher plant cell wall cellulose and in tunicates.

The crystal structure and the hydrogen bond system in cellulose I_β have been characterized by Nishiyama et al. (2002, 2003), Langan et al. (2005), Nishiyama et al. (2008, 2010). Here, we adopt the atomic coordinates for the cellulose I_β network A reported by Nishiyama et al. (2002). To account for the atomic positions inside the unit cell, we take advantage of the symmetry and antisymmetry operations provided by the crystallographic space group, commonly accepted to be monoclinic $P2_1$ (Sugiyama et al. 1991). Each crystallographic cell contains two molecular chains with a total of 42 ions per chain (84 ions per crystallographic cell). Note that the formula unit (f.u.) for this structure is $C_6O_5H_{10}$; there are two f.u.'s in the primitive cell and four in the crystallographic cell. Figure 2 depicts the crystalline structure reported by Nishiyama et al. (2002) after the symmetry operations are applied to the atomic coordinates. The represented structure was constructed using the *Crystalline cellulose—atomistic toolkit* (Zuluaga et al. 2013b). Intra- and inter-molecular hydrogen bonds are depicted in Fig. 2b following the hydrogen bond network A pattern reported in (Nishiyama et al. 2008; Šturcová et al. 2004). Cellulose chains are organized in hydrogen bonded planes (in the *b*–*c* plane) that are stacked together and held in position primarily by weak vdW interactions. Out-of-plane intermolecular hydrogen bonds, connecting cellulose chains in different planes, have also been reported (Matthews et al. 2012). Lattice parameters and crystallographic directions are superimposed in Fig. 2a, b for reference purposes. To facilitate our predictions of the anisotropy of the Young's modulus and Poisson's ratio of monoclinic cellulose I_β, we define a Cartesian system of coordinates *1*, *2* and *3*. Direction *1* is chosen to be parallel to *a* ([001]), and direction *3* is parallel to *c* ([001]). For the monoclinic $P2_1$ structure, *b* is not orthogonal to *a*. Therefore, direction *2* is chosen such that it is orthogonal to directions *1* and *3* as shown in Fig. 2a, b.

The lattice parameters for cellulose have been measured by several authors (Langan et al. 2005; Nishiyama et al. 2002, 2003, 2008, 2010; Sakurada et al. 1962, 1964; Matsuo et al. 1990; Sugiyama et al. 1991; Finkenstadt and Millane 1998) using different experimental techniques and crystal sources. For the cellulose I_β network A structure, Nishiyama et al. (2002) reported: $a = 7.784$ Å, $b = 8.201$ Å, $c = 10.380$ Å, $\alpha = 90°$, $\beta = 90°$, $\gamma = 96.55°$, with a 658.3 $Å^3$ volume at 293 K. Most of the measured lattice parameters exhibit variations around 1 % over a wide range of temperatures and crystalline sources, except for the lattice parameter *a*. As cellulose I_β is cooled or heated, the lattice remains remarkably constant in the directions within the hydrogen bonded planes containing the chains (i.e. *b* and *c*); the same is not true along the *a* axis direction where the contractions or expansions are controlled primarily by weak vdW interactions and interplanar hydrogen bonding (Wada et al. 2008; Langan et al. 2005). Nishiyama et al. (2008) reported a change from 7.64 to 7.76 Å in the *a* lattice parameter when the temperature was raised from 15 to 295 K. Langan et al. (2005) reported a value of 7.83 Å for the same parameter at 298 K. Although hydrogen bond interactions are present along the stacking direction (*a*-axis), they apparently do not prevent thermal expansion at temperatures up to the transition to a high-temperature phase at ~200 °C (Wada 2002; Bergenstråhle et al. 2007). This thermal sensitivity of the lattice parameter *a* should be kept in mind when comparing 0 K ab initio calculations with experimental values acquired at temperatures above 0 K. The temperature variation of the cellulose I_β structure is outside the scope of the current study, but it is reported elsewhere (Dri et al. 2013). Experimental lattice parameter and cell volume values, as well as ab initio simulation results, are summarized in Table 1.

Elastic stiffness matrix C_{ij} and compliance matrix S_{ij} for crystalline cellulose I_β

Materials that exhibit directional independence of their mechanical properties are referred to as isotropic. They have the advantage that their elastic response is characterized by only two parameters: the Young modulus (E) and the Poisson's ratio (ν). In addition, the stress–strain tensile behavior will be completely

Table 1 Ab initio and experimental lattice parameters (a, b, c, and γ) of cellulose I_β from different sources are listed

References	Methodology	Type of cellulose	a [Å]	b [Å]	c [Å]	γ [Deg]	Volume [Å^3]	Temp [K]
Sakurada et al. (1962)	X-Ray diffraction (XRD)	Bleached ramie (cellulose I)	7.9	8.35	10.3	96	675.7[a]	–
Sugiyama et al. (1991)	Electron diffraction	Green alga	8.01	8.17	10.36	97.3	672.5[a]	293
Finkenstadt and Millane (1998)	XRD	Valonia	7.85	8.27	10.38	96.3	669.8[a]	–
		(cellulose I_β)	7.82	8.16	10.32	97.5	652.9[a]	–
Nishiyama et al. (2002)	XRD and neutron fiber diffraction (NFD)	Tunicate	7.784	8.201	10.38	96.5	658.3	293
		(cellulose I_β)						
Langan et al. (2005)	XRD	Tunicate	7.76	8.19	10.38	96.51	655.4	100
		(cellulose I_β)	7.83	8.19	10.38	96.55	661.3	298
Nishiyama et al. (2008)	XRD and NFD	Tunicate	7.64	8.18	10.37	96.54	643.9	15
		(cellulose I_β)	7.76	8.20	10.37	96.62	655.5	295
Bučko et al. (2010)	PBE	Cellulose I_β	8.70	8.23	10.46	95.5	744.9	0
	PBE-D2		7.65	8.14	10.39	96.8	642.5	
Bučko et al. (2011)	PBE	Cellulose I_β network A	8.37	8.23	10.45	96.0	716	0
	PBE-D2		7.57	8.14	10.39	96.5	636	
	PBE-D2	Cellulose I_β network B	7.51	8.55	10.30	98.2	655	
Li et al. (2011)	LDA	Cellulose I_β	7.41	7.94	10.24	96.2	599.0[a]	0
	PBE		Not binding	8.27	10.54	94.7	–	
	PBE-D		7.85	8.18	10.47	96.6	667.9[a]	
This study	PBE-D2	Cellulose I_β network A	7.56	8.13	10.39	96.7	635	0

The double lines separate experimental results from simulations. Exchange–correlation functionals used in the ab initio simulations are: LDA (local density approximation), PBE (the generalized gradient approximation of Perdew–Burke–Ernzerhof or GGA-PBE) (Perdew et al. 1996); PBE-D and PBE-D2 (GGA-PBE with van der Waals corrections) (Kresse and Hafner 1994; Kresse and Furthmuller 1996a, b). See the "Computational methodology" section for additional details. The temperature at which each experiment was performed is reported in the last column. The symbol "–" means that the temperature was not reported

[a] Not reported, computed based on the lattice parameters

independent of the relative orientation of the specimen with respect to the loading direction. Anisotropic materials, however, exhibit variations in their mechanical properties with respect to an intrinsic direction within the material. One of the most common examples of a naturally-occurring anisotropic material is wood, were the grain is oriented along a particular direction. This significantly affects the mechanical response of the material. Hence, it is necessary to define a more general stress–strain relation for anisotropic solids that will account for mechanical property variations with direction within the material. The most general linear stress–strain relation for anisotropic materials is Hooke's Law, which has the form: $\sigma_{ij} = C_{ijkl}\,\varepsilon_{kl}$, where σ_{ij} and ε_{kl} represent the components of the second-order stress and strain tensors, respectively, and C_{ijkl} are the components of the fourth-order elasticity tensor with 81 components (Bower 2011). The inverse relation can also be written as $\varepsilon_{ij} = S_{ijkl}\,\sigma_{kl}$, where S_{ijkl} are the components of the elastic compliance tensor. These relationships can be converted to a matrix form based upon symmetries in C_{ijkl} and S_{ijkl}, leading to a stiffness matrix with components C_{ij} and a compliance matrix with components S_{ij}, both with 21 independent components (Bower 2011).

The monoclinic space group of cellulose I_β dictates that the unit cell has a symmetry plane that is defined

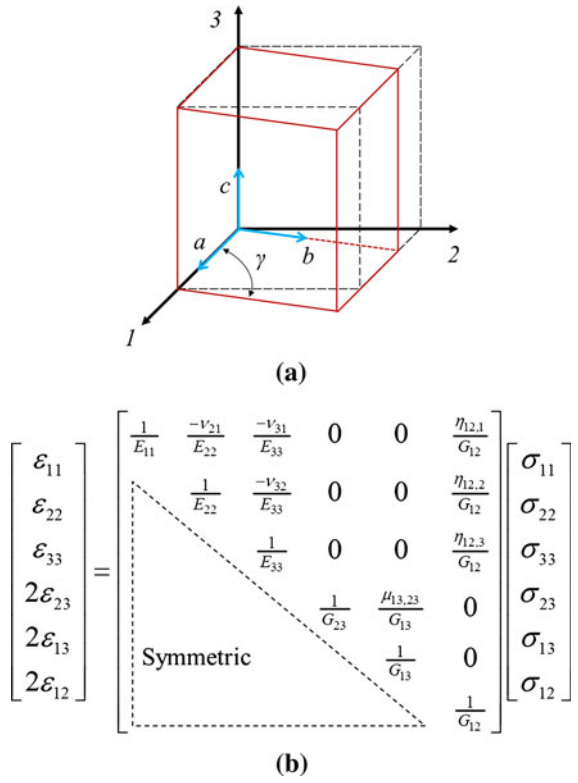

Fig. 3 **a** Schematic representation of the cellulose I_β monoclinic ($P2_1$) unit cell aligned with the Cartesian coordinate system used in this study (*red solid lines*). A rectangular prism cell (*black dashed lines*) is used to help visualize the orthogonally between the *a–c* and *b–c axes*, highlighting the non-orthogonal relationship between *a* and *b*. **b** Relationship between the strain and stress vectors via S_{ij} (Jones 1975) ($\varepsilon_{ij} = S_{ijkl}\,\sigma_{kl}$) for the $P2_1$ cellulose I_β unit cell. E_{ii} is the Young's modulus in the *i*-direction, G_{ij} is the shear modulus in the *i–j* plane, ν_{ij} is the Poisson's ratio which quantifies the contraction in the *j*-direction due to uniaxial loading in the *i*-direction, $\eta_{ij,k}$ are the coefficients of mutual influence of the first kind which characterize normal strain in the *k*-direction due to shear stress in the *i–j* plane, and $\mu_{ij,kl}$ are Chentsov's coefficients which characterize shear strain in the *k–l* plane due to shear stress in the *i–j* plane. (Color figure online)

by the *c*-axis. The presence of a symmetry plane has a direct consequence over the C_{ij} and S_{ij} in that it reduces the number of components necessary to represent the system. This leaves only 13 independent constants in each of C_{ij} and S_{ij}. Lastly, the matrix representation of the stress–strain relation must follow a coordinate system that allows a direct relationship between the matrix components and the cellulose I_β structure. Figure 3a shows a schematic representation of the main directions associated with the cellulose I_β unit cell and S_{ij} associated with the Cartesian system of coordinates denoted by axes *1*, *2* and *3*.

Figure 3b shows S_{ij} in terms of the Young's Modulus and Poisson's ratio in each direction for the $P2_1$ cellulose I_β unit cell (also appropriate for any monoclinic space group) (Jones 1975). With this information, three-dimensional surfaces can be constructed that are color contours of the Young's Modulus and Poisson's ratio. These contours follow variations of these properties with crystallographic direction. Additionally, 2D polar plots of the Young's Modulus and Poisson's ratio can be constructed which enable analysis of the variations of the Young's Modulus and Poisson's ratio with respect to a particular orientation angle within a given plane in the cellulose I_β unit cell.

Several relevant directions are depicted in Fig. 3a. For instance, E_{11}, E_{22} and E_{33} are the Young's moduli with respect to the directions *1*, *2* and *3*, respectively. It is important to note that E_{11} and E_{33} are the Young's moduli defined as the slope of the stress–strain curve produced in simple tension when the load is applied parallel to axes along *a* and *c*, respectively. Alternatively, E_{22} is defined along a direction determined by the cross product between the *a* and *c*-axes (i.e. *a–c* plane) (see Figs. 2 and 3a). In the *a–b* plane, two additional values of interest are defined, viz., $E_{[110]}$ and $E_{[010]}$, in which the subscripted indices represent the crystallographic direction defined by the Miller indices. Note that $E_{[110]}$ is along the axis that runs through the center chain in the unit cell (see Fig. 2a), whereas $E_{[010]}$ is aligned with the *b*-axis. The Poisson's ratio is also reported using a similar nomenclature; for example, ν_{12} is the Poisson's ratio for the contraction in the *2*-direction due to uniaxial loading in the *1*-direction. It is common to report an average value of the Poisson's ratio using the two perpendicular directions with respect to the loading direction. Hence, only one index is needed. For the direction *1*, this is defined as

$$\bar{\nu}_1 = \frac{\nu_{12} + \nu_{13}}{2} \tag{1}$$

Computational methodology

All calculations in this study were conducted with the Vienna Ab initio Simulation Package (VASP), a plane wave DFT code (Kresse and Hafner 1994; Kresse and

Furthmuller 1996a, b; Hafner 2008). The electron–ion interactions were described by the full potential projector augmented wave (PAW) method (Blöchl 1994). Exchange–correlation was treated within the generalized gradient approximation of Perdew, Burke and Ernzerhof (GGA-PBE) (Perdew et al. 1996). Standard density functionals within the GGA or LDA cannot correctly describe vdW interactions resulting from dynamical correlations between fluctuating charge distributions (Bučko et al. 2010). This makes them intrinsically unsuitable for computing structural parameters of cellulose I_β. Using PBE functionals, Bučko et al. (2010, 2011) reported a value of a that is overestimated by $\sim$15 % compared to experimental results at 15 K (Nishiyama et al. 2008). Li et al. (2011) found that cellulose fails to retain its crystalline structure when using PBE functionals (see Table 1 for more information). In order to circumvent this problem, a semi-empirical correction for the vdW interactions [now incorporated as PBE-D and PBE-D2 in VASP (Kresse and Hafner 1994; Kresse and Furthmuller 1996a, b)] was proposed by Grimme and coworkers (Grimme 2006; Antony and Grimme 2006). Using this dispersion-corrected DFT method (PBE-D2), Bučko et al. (2010, 2011), Li et al. (2011) and Parthasarathi et al. (2011) showed that vdW and hydrogen bonding interactions play an equally important role in defining the final shape of the cellulose I_β monoclinic ($P2_1$) structure and hence they cannot be neglected. Therefore, all calculations in this study are conducted using the dispersion corrected PBE-D2 in VASP (Bučko et al. 2010, 2011).

Structural parameters and mechanical property calculations were computed by simultaneously minimizing all atomic forces and stress tensor components via a conjugate gradient method. The results presented in this work were obtained using a simulation cell corresponding to one crystallographic cell of cellulose I_β, following the structure reported by Nishiyama et al. (2002). Three successive full-cell optimizations were conducted (adapting basis vectors and computational grids to the cell parameters) to ensure convergence of cell energies and structural parameters. Total energies were calculated for the relaxed cellulose I_β structure by integrating over a Monkhorst–Pack mesh of k-points in the Brillouin zone with the linear tetrahedron method with Blöchl corrections. The plane wave cutoff energy for all calculations was 500 eV. The total energy was converged to 10^{-7} eV/cell and the force components were relaxed to at least 10^{-4} eV/Å. For all calculations (i.e. structural and elastic properties), a $7 \times 7 \times 7$ k-point mesh, corresponding to a k-point spacing of $0.110 \times 0.086 \times 0.110$ per Angstrom, was used.

Components of the stiffness matrix, C_{ij}, were computed from the first derivatives of the stresses computed in VASP, rather than from the second derivatives of the total energy with respect to strain, using the Le Page and Saxe least squares method (Le Page and Saxe 2002). This method avoids the numerical difficulties often encountered with evaluations of the latter and reduces the number of required VASP calculations. All C_{ij} values were computed simultaneously rather than as independent sums. The C_{ij} are sensitive to the k-point mesh, and this required a series of ancillary calculations to test k-point convergence of each of the 13 unique C_{ij} for the monoclinic cellulose I_β structure. In addition, it was determined that the application of four successive strains, viz., 0.05, 1.0 1.5, and 2.0 % was adequate to obtain $\leq$1.0 % statistical error in each C_{ij}. The quality of the least squares fit, as gauged by the computed least squares residual, was $\leq$1.0 % for all calculations. The small residuals are consistent with negligible anharmonic effects in the computed C_{ij} due to the applied strains. Note that the Le Page and Saxe method for computing elastic properties with DFT has been successfully used to compute elastic properties for a wide variety of materials, including hydrides (Hector et al. 2003, 2007; Hector and Herbst 2004), batteries (Qi et al. 2010; Shang et al. 2012), ceramics (Qi and Hector 2004; Qi and Hector 2007), metals (Shang et al. 2009; Wróbel et al. 2012) and defects (Woodward et al. 2008). Once the stiffness matrix was computed, it was subsequently inverted to obtain the compliance matrix, S_{ij}. As explained in the previous section, the C_{ij} and the S_{ij} depend on the definition of the coordinate system chosen for the simulations. We use rotation techniques, such as those detailed in Bower (2011), which allow us to convert the computed compliance matrix to any desired orientation. The basis change follows from

$$S^{(1'2'3')} = K^{-T} S^{(123)} K^{-1} \tag{2}$$

For the particular case of rotation through an angle θ in a counterclockwise sense about the *1*, *2* and *3* axes, respectively, the rotation matrix K reduces to

$$
\begin{bmatrix}
1 & 0 & 0 & 0 & 0 & 0 \\
0 & c^2 & s^2 & 2cs & 0 & 0 \\
0 & s^2 & c^2 & -2cs & 0 & 0 \\
0 & -cs & cs & c^2 - s^2 & 0 & 0 \\
0 & 0 & 0 & 0 & c & -s \\
0 & 0 & 0 & 0 & s & c
\end{bmatrix}
\begin{bmatrix}
c^2 & 0 & s^2 & 0 & 2cs & 0 \\
0 & 1 & 0 & 0 & 0 & 0 \\
s^2 & 0 & c^2 & 0 & -2cs & 0 \\
0 & 0 & 0 & c & 0 & -s \\
-cs & 0 & cs & 0 & c^2 - s^2 & 0 \\
0 & 0 & 0 & s & 0 & c
\end{bmatrix}
\begin{bmatrix}
c^2 & s^2 & 0 & 0 & 0 & 2cs \\
s^2 & c^2 & 0 & 0 & 0 & -2cs \\
0 & 0 & 1 & 0 & 0 & 0 \\
0 & 0 & 0 & c & s & 0 \\
0 & 0 & 0 & -s & c & 0 \\
-cs & cs & 0 & 0 & 0 & c^2 - s^2
\end{bmatrix} \tag{3}
$$

where $c = \cos(\theta)$ and $s = \sin(\theta)$. Clearly, applying the three rotations successively can produce an arbitrary orientation change. This provides the basis to construct the 3D surface contour plots and polar plots of the angular variation of the Young's Modulus and Poisson's ratio. .

Results and discussion

Results from VASP calculations with the semi-empirical correction for the vdW interactions were used to generate the surface contour plot of the Young's modulus variation with crystallographic direction shown in Fig. 4a. This is based upon Eqs. (2) and (3) and the S_{ij} computed from application of 1.0 % strain in the Le Page and Saxe method (Le Page and Saxe 2002). A post processing software package, the *Anisotropy Calculator—3D Visualization Toolkit*, was specifically developed to generate the surface contour plot of the Young's modulus based on S_{ij} and is now publically available (Zuluaga et al. 2013a). Each point on the surface represents the magnitude of Young's modulus in the direction of a vector from the origin of the surface (i.e. at the intersection of the *1*, *2* and *3* axes in the interior of the surface) to a given point on the surface. The shape of this surface is indicative of the anisotropy of cellulose I_β. For instance, the computed Young modulus surface for a linearly elastic isotropic material would be a perfect sphere with the same value in any direction. However, the cellulose I_β surface in Fig. 4a exhibits extreme variations in the Young's modulus, as denoted by the accentuated contour lobe along the *3*-axis (i.e. along the cellulose chains) relative to the smaller lobes along the *1* and *2* directions. The largest values (red contours) are along the *3*-axis, with the smallest values along the *1*-axis. The greatest value of the Young's modulus is 206 GPa, which is comparable to that of steel ($\sim$207 GPa) (Leslie 1981). Figure 4b, c and d show side views of the same surface in Fig. 4a to put in evidence the differences in Young's moduli for directions lying on the *1–2*, *1–3* and *2–3* planes in better perspective.

Polar plots of the angular variation of the Young's modulus within a given crystallographic plane of the monoclinic cellulose I_β crystal structure are shown in Figs. 5 and 6. These plots can be used to help provide insight into the variability in the reported experimental values (ranging from 90 to 220 GPa) of the Young's modulus. Figure 5 shows the angular variation of the Young's modulus along the *1–3* plane (as shown by the gray plane in the inset on the upper left of the figure). Three axes are considered: direction *1* (which is the vertical axis), direction *3* (the horizontal axis) and the semi-circular line showing the angle with respect to the origin. These are the same axes defined in Figs. 2 and 3a. The scale of the vertical axis denotes the magnitude of E_{11}, whereas the scale of the horizontal axis denotes the magnitude of E_{33}. The inset in the bottom semi-circular part shows the orientation of the directions *1* and *3* with respect to the cellulose I_β unit cell. Here, θ is the angle between the *3′*-direction, along which the load is applied, and the *3*-direction (in the *1–3* plane). The plot is generated by computing S_{ij} for different angles using Eqs. (2) and (3), and extracting the Young modulus value in the *3′*-direction from the rotated compliance matrix. Components of the S_{ij}, computed in the Cartesian coordinate system shown in Fig. 3a were obtained following the Le Page and Saxe method (Le Page and Saxe 2002) for three values of applied strains, viz. 1.0 1.5, and 2.0 %. A change of only 10° in the longitudinal alignment (*c*-axis) reduces the DFT-predicted Young modulus from 206 to $\sim$70 GPa. This considerable reduction is related to the deformation mechanism in which the cellulose I_β structure is under simple tension in each of the *1*, *2*, *3* directions.

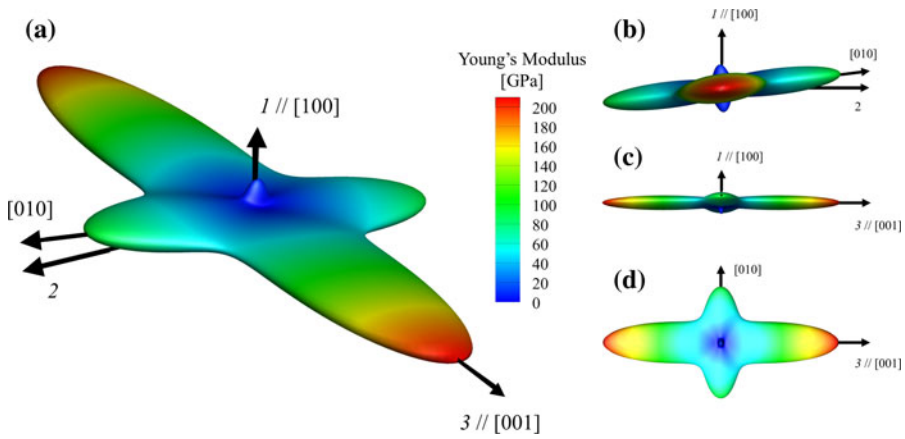

Fig. 4 **a** Surfaces showing contours of computed Young's modulus values for cellulose I_β based on an S_{ij} from application of a 1 % strain in the Le Page and Saxe method (Le Page and Saxe 2002). Each point on the surface represents the magnitude of the Young's modulus in the direction of a vector from the origin of the surface to that point. The *color contours* help to identify the Young modulus variation of cellulose I_β and emphasizes its extreme anisotropy (note the significant elongation of the surface along axis 3). Side views of the same surface are shown for the **b** *1–2* plane, **c** *1–3* plane, **d** *2–3* plane. Note that axis *2* is not seen in these additional views. (Color figure online)

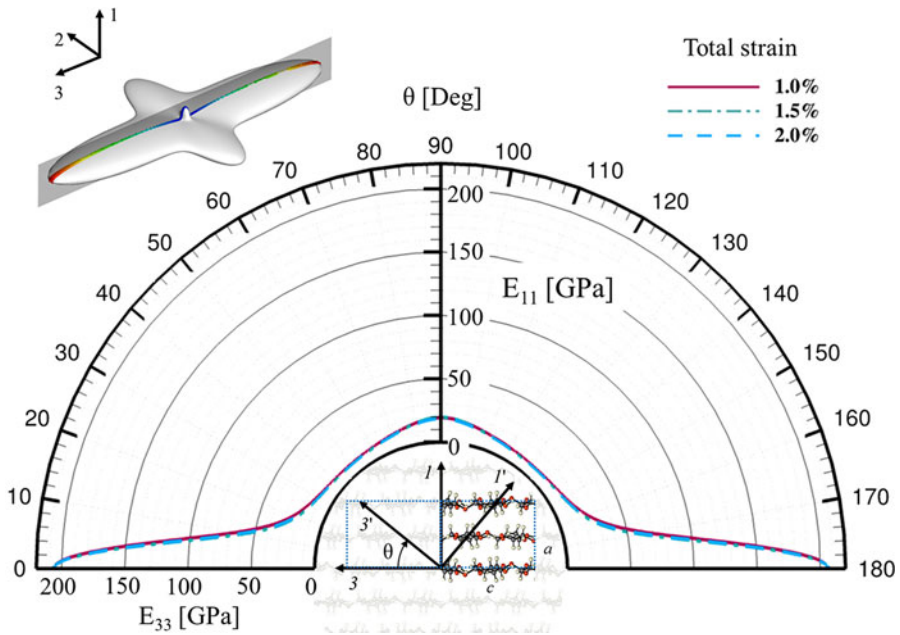

Fig. 5 Angular variation of the longitudinal Young's modulus (E_A) within the *1–3* plane for applied strains of 1.0, 1.5, and 2.0 %. The *2*-axis (perpendicular to the page) is considered to be the rotation axis; the value of the longitudinal modulus for a given direction can be read directly from the figure by defining a *straight line* from the origin to the desired angle. It is important to notice how small misalignments between the cellulose I_β *c*-axis and the *3*-direction will produce an important reduction in the interpretation of E_A during experimental characterization. The *inset* in the *bottom* semi-circular part shows the orientation of the *1* and *3* directions with respect to the cellulose I_β unit cell

For instance, imposing a deformation perfectly aligned with the *c*-direction involves a series of very complex deformation mechanisms. Among them we found stretching of the covalent bonds between C and O ions that form the cellulose chain (shown as the ball and stick features Fig. 2), stretching of intra-

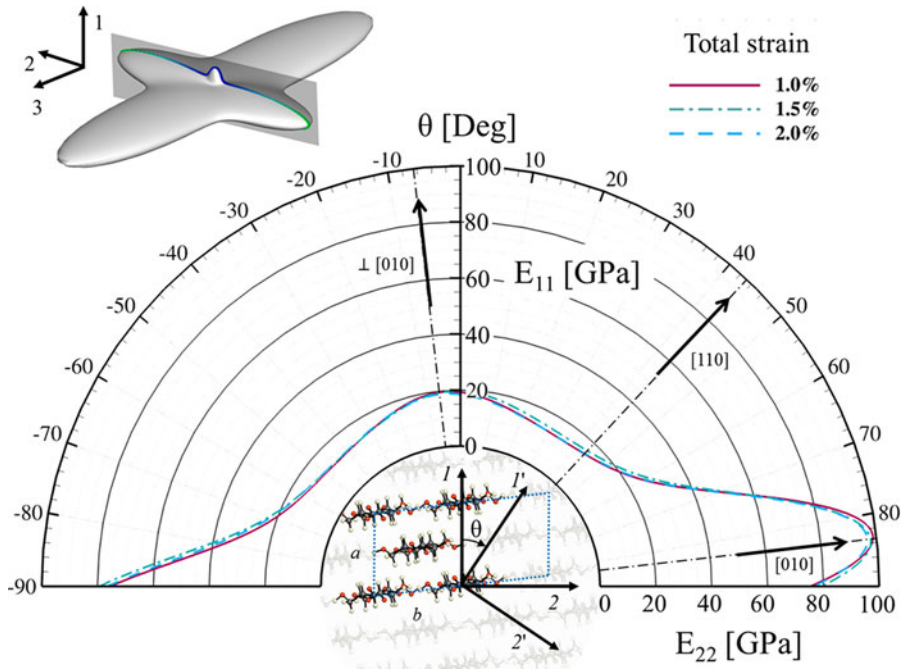

Fig. 6 Angular variation of the E_T at applied strains of 1.0, 1.5, and 2.0 %. The *3*-axis (pointing perpendicular to the page) is considered to be the rotation axis; the value of E_T for a given direction can be read directly from the figure by defining a straight line from the origin to the desired angle. The intersection between the *straight line* and the *curves* for different strains provides the value of E_T. Three critical directions (// to *b*, through the center chain and ⊥ to *b*) are marked for reference using Miller indices; the direction parallel to the *a*-axis coincides with the *vertical axis* of the figure. The superposition of the three strain curves allow us to concluded that the crystal behaves linearly for strains up to 2 %. The *inset* in the *bottom* semi-circular part shows the orientation of the *1* and *2* directions with respect to the cellulose I_β unit cell

molecular hydrogen bonds (shown as green dashed lines in Fig. 2), angle bending, rotations and distortions. This results in the highest value of the Young modulus (206 GPa) along the *c*-direction (the *3*-direction). In the *a*-direction (which corresponds to the *1*-direction), hydrogen bonded planes are stacked together and held in position primarily by weak vdW interactions. Any deviation of the stretching direction in the *1–3* plane will produce a rapid decrease in the Young's modulus due to sliding between adjacent planes. In the *b*-direction, the intermolecular hydrogen bonds (See Fig. 2b) provide additional reinforcement to keep the cellulose chains from sliding. As a consequence, the effects of misalignments on the resulting Young's modulus in any direction lying on the *2–3* plane are less severe compared with those in the *1–3* plane. Note that deviations between the curves from the applied strains, viz. 1.0, 1.5, and 2.0 % are very minimal, as it can be observed in Figs. 5 and 6.

Upon comparing our DFT-computed results with experimental data (Table 2), E_{33} can be regarded as the axial Young's modulus (E_A). However, the experimental value of E_T can be interpreted as any of the Young's moduli in any of the directions lying in the *1–2* plane. Figure 6 is polar plot that shows the variation of the Young's modulus with angular orientation within the *1–2* plane. Here, θ is the angle between the *1′*-direction, along which the load is applied, and the *1*-direction (in the *1–2* plane). The plot is generated by computing S_{ij} for different angles using Eqs. (2) and (3) and extracting the Young modulus value in the *1′*-direction from the rotated S_{ij}. Stretching in the *b*-direction implies separating chains in the hydrogen bonded planes which explains why $E_{[010]}$ has the highest value for E_T (98 GPa). Perpendicular to the *b*-direction (marked as ⊥[010] in Fig. 6), non-bonded interactions have to be overcome to increase the distance between adjacent planes, producing a relative maximum (19 GPa) in the Young's modulus. Another observation is that E_T reaches its minimum (13 GPa) between the *b*-direction and the direction perpendicular to the *b*-direction ($\sim 30°$ in the plot). This could

Table 2 Summary of Young's modulus and Poisson's ratio values from different crystalline sources and authors

References	Methodology	Type of cellulose	E_A [GPa]	E_T [GPa]	ν_t	Temp [K]
Sakurada et al. (1962), (1964), Matsuo et al. (1990), Nishino et al. (1995), Ishikawa et al. (1997)	X-Ray diffraction (XRD)	Ramie (cellulose I)	90–138	–	–	–
Nakamura et al. (2004)	XRD	Ramie fiber (cellulose I_β)	–	–	$\nu_{[200]/[004]} = 0.377 \pm 0.041$[b] $\nu_{[110]/[004]} = 0.639 \pm 0.338$[b]	Room Temp
Diddens et al. (2008)	Inelastic X-ray (IXR)	Flax fibers (cellulose I_β)	220 ± 50	14.8 ± 0.8	–	–
Wagner et al. (2011)	Atomic force microscope (AFM)	Tunicate CNC	–	2.7–20	–	–
Pakzad et al. (2012)	AFM + finite elements	Wood CNC	–	24.8 ± 7.0	–	–
		Cotton CNC		17.7 ± 5.0		
Matsuo et al. (1990), Tashiro and Kobayashi (1991)	Theoretical derivation	Cellulose I	167.5	$E_{t1} = 50.2$[a] $E_{t2} = 10.6$[a]	$\nu = 0.42$[a]	–
Eichhorn and Davies (2006)	Molecular mechanics (MM) [COMPASS]	Cellulose Iβ—Nishiyama	149	$E_{t1} = 46.8$[a] $E_{t2} = 18.9$[a]	$\nu = 0.439$[a]	Min[c]
		Cellulose Iβ—Finkenstadt	116	$E_{t1} = 50.9$[a] $E_{t2} = 11.9$[a]	$\nu = 0.86$[a]	
Santiago Cintrón et al. (2011)	Quantum mechanics [B3LYP/6-311G**+]	1,40-*O*-dimethyl-b-cellobioside	99.7	–	–	–
Wu et al. (2013)	Molecular dynamics (MD) [ReaxFF]	Cellulose Iβ	139.5 ± 3.5	$E_{t1} = 28.8 \pm 2.9$ $E_{t2} = 7.0 \pm 1.7$	–	300 K

The double line in the table separates experimental from theoretical results. The symbol "–" means that the corresponding value was not reported

[a] Not reported, computed based on reported S_{ij} or C_{ij}

[b] Upper limit of the standard deviation

[c] The authors perform energy minimization without specifying any temperature

be caused by the relative sliding between hydrogen bonded planes. Based on Fig. 6, it can be estimated that there is a 65 % probability of measuring E_T under 20 GPa during experimental measurements; misalignments in the *c*-direction could increase this probability. Our simulations at 0 K yielded values from 13 to 98 GPa, which are in good agreement with reported experimental results (Diddens et al. 2008; Wagner et al. 2011; Pakzad et al. 2012; Lahiji et al. 2010) and numerical simulations (Matsuo et al. 1990; Eichhorn and Davies 2006; Wu et al. 2013). A summary is shown in Table 2. The calculated Young's moduli in selected directions are reported for different total strains [applied in the Le Page and Saxe method (Le Page and Saxe 2002)] in Table 3.

The variation of the average Poisson's ratio $\bar{\nu}_{1'}$ with respect to any arbitrary direction $1'$ was computed from the S_{ij} by applying Eq. (1) to the rotated

Table 3 Young's moduli as a function of orientation for applied strains of 1.0, 1.5, and 2.0 % from DFT calculations in the present study

Young's modulus	Total strain			Average
	1.0 %	1.5 %	2.0 %	
E_{33}	206.7	206.7	206.2	206.5
E_{11}	19.3	19.7	18.5	19.1
$E_{\perp[010]}$	19.6	19.4	18.9	19.3
$E_{[110]}$	14.8	16.3	15.0	15.3
$E_{[010]}$	98.7	97.9	96.7	97.8
E_{22}	75.4	79.2	76.4	77.0

This table summarizes the results shown in Fig. 6. Young's modulus are reported in GPa, computed at 0 K using DFT with van der Waals interactions (this work)

compliance matrix obtained using Eqs. (2) and (3). Here the *1′*-direction indicates the orientation of the load (which is the orientation that is being evaluated). Figure 7a shows one view of the computed $\bar{\nu}_{1'}$ surfaces. Figure 7b–d show views of the same surface in the *1–2*, *1–3*, and *2–3* planes, respectively. These results clearly show the strong variations in $\bar{\nu}_{1'}$ with minimum values along the directions [100], [010] and [001]. As it can be observed in Fig. 7, the type of anisotropy in $\bar{\nu}_{1'}$ is different from that shown for the Young's Modulus (Fig. 4). The details on how $\bar{\nu}_{1'}$ varies in some selected planes will be discussed next (Table 4).

Table 4 Computed Poisson's ratio values, as a function of the orientation with respect to the Cartesian system of coordinates *1–2–3*, for different total strains

Poisson's ratio	Total strain applied in the Le Page and Saxe method (Le Page and Saxe 2002)			Average over strains
	1.0 %	1.5 %	2.0 %	
ν_{12}	0.143	0.130	0.148	0.140 ± 0.010
ν_{13}	0.042	0.042	0.039	0.041 ± 0.002
$\bar{\nu}_1$	0.092	0.086	0.094	0.091 ± 0.005
$\nu_{\perp[010]/[010]}$	0.107	0.111	0.114	0.111 ± 0.003
$\nu_{\perp[010]/[001]}$	0.048	0.046	0.044	0.046 ± 0.002
$\bar{\nu}_{\perp[010]}$	0.077	0.078	0.079	0.078 ± 0.001
$\nu_{[110]/\perp[\bar{1}\bar{1}0]}$	0.715	0.714	0.683	0.704 ± 0.021
$\nu_{[110]/[001]}$	0.004	0.003	0.004	0.004 ± 0.001
$\bar{\nu}_{[110]}$	0.360	0.359	0.344	0.354 ± 0.010
$\nu_{[010]/\perp[0\bar{1}0]}$	0.537	0.558	0.586	0.560 ± 0.026
$\nu_{[010]/[001]}$	0.024	0.025	0.026	0.025 ± 0.001
$\bar{\nu}_{[010]}$	0.280	0.291	0.306	0.292 ± 0.014

This table summarizes the results shown in Fig. 8

Figure 8 shows a polar plot of $\nu_{1'2'}$, $\nu_{1'3}$ and $\bar{\nu}_1$ using the *c*-axis as the rotation axis, in which variations of these quantities are examined over the *1–2* plane (where θ is the angle between the *1′*-direction, along which the load is applied, and the *1*-direction in the *1–*

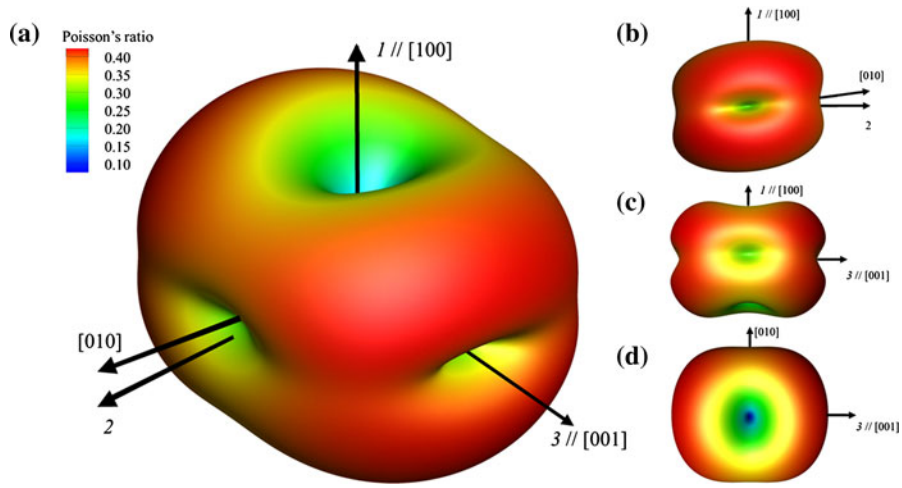

Fig. 7 Average Poisson's ratio $\bar{\nu}_{1'}$ surfaces for cellulose I_β computed using Eq. 1 based on S_{ij} for 1.0 % of total deformation in the Le Page and Saxe method (Le Page and Saxe 2002). Each point on the surface represents the magnitude of Poisson's ratio in the direction of a vector from the origin to that point. The *color contours* help to identify the Poisson's ratio variation and emphasizes the extreme anisotropy of the system. Side views of the same surface are shown for the **b** *1–2* plane, **c** *1–3* plane, **d** *2–3* plane. Note that axis *2* is not seen from this view. (Color figure online)

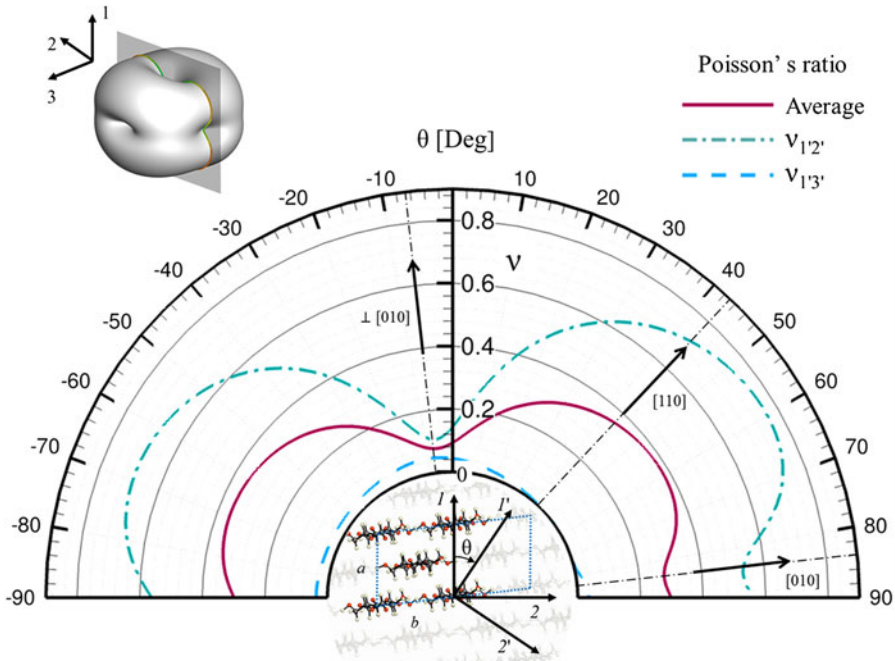

Fig. 8 Poisson's ratio as a function of the rotation angle for 1.0 % of total strain. The *inset* in the *upper-left corner* depicts the surface of the average Poisson's ratio as shown in Fig. 7 and the selected plane in which the polar plot lies. The *3*-axis (pointing perpendicular to the page) is considered to be the rotation axis; the value of the Poisson's ratio for a given direction can be read directly from the figure by defining a straight line from the origin to the desired angle. The intersection between the *straight line* and the *curves* provide the values of $\nu_{1'2'}$, $\nu_{1'3}$ and the average of them ($\bar{\nu}_{1'}$) for that direction. Three critical directions (// to *b*, through the center chain and $\perp$ to *b*) are marked for reference using Miller indices; the direction parallel to the *a*-axis coincides with the *vertical axis* of the figure

Fig. 9 Elastic compliance (*S*) and stiffness (*C*) matrices for cellulose I_β based upon the Nishiyama et al. (2002) initial structure with respect to the Cartesian system of coordinates shown in Fig. 3a. All components were computed using the Le Page and Saxe method with with the dispersion-corrected DFT method (PBE-D2) in VASP for three different total strains (1.0, 1.5 and 2.0 %). Values of *S* are given in [1/GPa] × 1000, and those for *C* are in [GPa]

$$S_{1.0\%} = \begin{bmatrix} 51.9 & -7.4 & -2.2 & 0.0 & 0.0 & 11.2 \\ & 13.3 & -0.5 & 0.0 & 0.0 & -25.6 \\ & & 4.8 & 0.0 & 0.0 & 2.2 \\ & & & 60.0 & -43.3 & 0.0 \\ & \text{Symmetric} & & & 372.7 & 0.0 \\ & & & & & 239.7 \end{bmatrix} \quad C_{1.0\%} = \begin{bmatrix} 21.5 & 13.0 & 11.0 & 0.0 & 0.0 & 0.3 \\ & 102.8 & 11.3 & 0.0 & 0.0 & 10.2 \\ & & 213.3 & 0.0 & 0.0 & -1.3 \\ & & & 18.2 & 2.1 & 0.0 \\ & \text{Symmetric} & & & 2.9 & 0.0 \\ & & & & & 5.3 \end{bmatrix}$$

$$S_{1.5\%} = \begin{bmatrix} 50.9 & -6.6 & -2.1 & 0.0 & 0.0 & 3.6 \\ & 12.6 & -0.5 & 0.0 & 0.0 & -21.4 \\ & & 4.8 & 0.0 & 0.0 & 2.3 \\ & & & 60.9 & -26.5 & 0.0 \\ & \text{Symmetric} & & & 427.8 & 0.0 \\ & & & & & 222.7 \end{bmatrix} \quad C_{1.5\%} = \begin{bmatrix} 21.7 & 13.1 & 10.5 & 0.0 & 0.0 & 0.8 \\ & 102.8 & 11.8 & 0.0 & 0.0 & 9.5 \\ & & 213.1 & 0.0 & 0.0 & -1.3 \\ & & & 16.9 & 1.0 & 0.0 \\ & \text{Symmetric} & & & 2.4 & 0.0 \\ & & & & & 5.4 \end{bmatrix}$$

$$S_{2.0\%} = \begin{bmatrix} 54.1 & -8.0 & -2.1 & 0.0 & 0.0 & 11.5 \\ & 13.1 & -0.5 & 0.0 & 0.0 & -23.2 \\ & & 4.8 & 0.0 & 0.0 & 2.1 \\ & & & 62.2 & -31.6 & 0.0 \\ & \text{Symmetric} & & & 411.9 & 0.0 \\ & & & & & 229.8 \end{bmatrix} \quad C_{2.0\%} = \begin{bmatrix} 20.8 & 13.5 & 10.4 & 0.0 & 0.0 & 0.2 \\ & 102.1 & 12.0 & 0.0 & 0.0 & 9.5 \\ & & 212.5 & 0.0 & 0.0 & -1.3 \\ & & & 16.7 & 1.3 & 0.0 \\ & \text{Symmetric} & & & 2.5 & 0.0 \\ & & & & & 5.3 \end{bmatrix}$$

2 plane). In order to quantify lateral deformation, we define a local Cartesian system *1′–2′* that rotates with respect to the *1* and *2* directions and remains in the *1–2* plane. First, $\nu_{1'2'}$ provides the lateral deformation in the *2′*-direction as uniaxial stress is applied along the *1′*-direction. It is important to remember that the *2′*-direction rotates perpendicular to the *1′*-direction in the *1–2* plane in Fig. 8. The smallest value of $\nu_{1'2'} \approx 0.1$ is found when the *1′*-direction is aligned with the direction marked as $\perp$[010] in the plot. This happens to be the direction perpendicular to the hydrogen bonded planes which contain the cellulose chains. This small value is expected since increasing the separation between hydrogen bonded planes, held together primarily by weak vdW interactions, has little effect over the arrangement of the cellulose chains inside the plane. The next local minimum is found to be in the [010]-direction where the opposite effect is observed. Trying to separate cellulose chains from each other has little effect over the arrangement of hydrogen bonded planes. The axial deformation of the system shows a different behavior. Here, $\nu_{1'3}$ measures the contraction in the *3*-direction as uniaxial stress is applied in the *1′*-direction (since the *1′* and the *2′* directions remain in the *1–2* plane, the *3′*-direction coincides with the *3* direction). In Fig. 8, the *3*-direction coincides with the rotation axis (perpendicular to the plane of the plot), meaning that this direction is always coincident with the cellulose chain regardless of the orientation angle. The small values of $\nu_{1'3}$ for all directions (ranging from 0 to 0.05) can be easily justified by the covalent bonds between carbon and oxygen ions that govern the mechanical response in the *c*-direction: these are largely unaffected by deformation in other directions. When the cellulose I_β is deformed along a direction that passes near the center chain (around 45° in the plot), practically no Poisson effect (no lateral expansion in the *3*-direction) is observed in the axial direction (Fig. 8).

The extreme anisotropies observed in cellulose I_β can be once again evidenced in the high variations of the Poisson's ratio. Depending on the selected direction, the Poisson's ratio will range from almost 0 to 0.71. Comparison with previous publications (Matsuo et al. 1990; Eichhorn and Davies 2006; Nakamura et al. 2004) shows results that are in good agreement with the values reported in this study. Finally, our computed C_{ij} and S_{ij}, based on the Cartesian system shown in Fig. 2, are reported for each applied strain in Fig. 9.

Conclusion

The full elasticity tensor was computed for cellulose I_β network A using DFT with van der Waals interactions using a least squares fitting method with VASP as the computational engine. Our results show a good agreement with previous experimental work, in particular, a remarkable agreement is found with the IXS experiments conducted by Diddens et al. (2008). Three dimensional surfaces, which are color contours showing the crytstallographic dependence of the Young's modulus and Poisson's ratio, were computed to examine the extreme anisotropy of these important elastic properties. A clear correlation between the stiffness of the crystal and the different deformation mechanisms was noted. The largest Young's modulus (206 GPa) was found to be aligned with the *c*-axis were covalent bonds dominate the mechanical response of the crystal. Perpendicular to the cellulose chain axis, the *b*-direction shows the next greatest value for the Young modulus (98 GPa); this can be explained by the presence of the hydrogen bond network linking the cellulose chains. Finally, a value for the Young modulus of only 19 GPa was computed along the direction perpendicular to the previous two, where weak vdW interactions play a dominant role in the mechanical response of the material. Based on our 0 K simulations with dispersion-corrected DFT in VASP, the transverse Young Modulus for crystalline cellulose can be defined in the range between 13 and 98 GPa, in good agreement with reported experimental results (Diddens et al. 2008; Wagner et al. 2011; Pakzad et al. 2012; Lahiji et al. 2010) and other numerical simulations (Matsuo et al. 1990; Eichhorn and Davies 2006; Wu et al. 2013).

It should be mentioned that the predicted values of Young's modulus along the *c*-axis in this work is higher than the $\sim$100–150 GPa range usually reported in other numerical works (Matsuo et al. 1990; Tashiro and Kobayashi 1991; Eichhorn and Davies 2006; Wu et al. 2013). While the origins of this discrepancy between previous molecular dynamics calculations and the present DFT results is not known, some additional comments on this issue are warranted. Molecular dynamics calculations are sensitive to the force field being used. These usually involve semi-empirical potentials for the bonding interactions between the elemental constituents. As such they do not explicitly account for electron exchange and correlation as DFT does. Alternatively, a potential contributing factor from

DFT may be the choice of the exchange–correlation functional, for which we chose the gradient-corrected formalism of Perdew, Burke and Ernzerhof (GGA-PBE) (Perdew et al. 1996). However, the GGA approach is known to predict mechanical properties that are closer to those reported in experimental works than those predicted by local density formalisms (Hector et al. 2007). Moreover, future DFT studies of cellulose will focus on exploring HSE06 functionals (Heyd et al. 2003, 2006), which allow exact exchange, rather than the approximations involved with other DFT functionals. These recent functionals mix the DFT and Hartree–Fock approaches and have been shown to give more accurate predictions of band gaps, for example, relative to the local density or gradient corrected approximations. The extent to which HSE06 functionals influence predicted mechanical properties for materials such as cellulose relative to a gradient corrected functional, such as that used herein, is currently unknown.

Acknowledgments The authors wish to acknowledge the staff of the High Performance Computing Center at General Motors. Additional computational resources, networking, and support were provided by GM Information Systems and Services. R.J.M. and P.D.Z. are also grateful to financial support by the Forest Products Laboratory under USDA Grants: 11-JV-11111129-086, 07-CR-11111120-093, the Purdue Research Foundation and National Science Foundation through Grant No. CMMI-1131596.

References

Antony J, Grimme S (2006) Density functional theory including dispersion corrections for intermolecular interactions in a large benchmark set of biologically relevant molecules. Phys Chem Chem Phys 8(45):5287–5293. doi:10.1039/b612585a

Azizi Samir MAS, Alloin F, Dufresne A (2005) Review of recent research into cellulosic whiskers, their properties and their application in nanocomposite field. Biomacromolecules 6(2):612–626

Bergenstråhle M, Berglund LA, Mazeau K (2007) Thermal response in crystalline Iβ cellulose: a molecular dynamics study. J Phys Chem B 111(30):9138–9145. doi:10.1021/jp072258i

Blöchl PE (1994) Projector augmented-wave method. Phys Rev B 50(24):17953–17979

Bower AF (2011) Applied mechanics of solids. CRC press, Boca Raton, FL

Bučko T, Hafner J, Lebègue S, Ángyán JG (2010) Improved description of the structure of molecular and layered crystals: ab initio DFT calculations with van der Waals corrections. J Phys Chem A 114(43):11814–11824. doi:10.1021/jp106469x

Bučko T, Tunega D, Ángyán JG, Hafner J (2011) Ab initio study of structure and interconversion of native cellulose phases. J Phys Chem A 115(35):10097–10105. doi:10.1021/jp205827y

Diddens I, Murphy B, Krisch M, Müller M (2008) Anisotropic elastic properties of cellulose measured using inelastic X-ray scattering. Macromolecules 41(24):9755–9759. doi:10.1021/ma801796u

Dri F, Shang S, Hector LG Jr, Zi-Kui Liu, Moon RJ, Zavattieri PD (in preparation, 2013) Study of thermodynamic and mechanical properties of crystalline cellulose

Eichhorn SJ, Davies GR (2006) Modelling the crystalline deformation of native and regenerated cellulose. Cellulose 13(3):291–307. doi:10.1007/s10570-006-9046-3

Finkenstadt VL, Millane RP (1998) Crystal structure of valonia cellulose Iβ. Macromolecules 31(22):7776–7783. doi:10.1021/ma9804895

Grimme S (2006) Semiempirical GGA-type density functional constructed with a long-range dispersion correction. J Comput Chem 27(15):1787–1799. doi:10.1002/jcc.20495

Hafner J (2008) Ab-initio simulations of materials using VASP: density-functional theory and beyond. J Comput Chem 29(13):2044–2078

Hector LG Jr, Herbst JF (2004) Electronic and elastic properties of RCo5 and RCo5Hn (R = La, Ce, Pr). J Alloy Compd 379(1–2):41–53. doi:10.1016/j.jallcom.2004.02.042

Hector LG Jr, Herbst JF, Capehart TW (2003) Electronic structure calculations for LaNi5 and LaNi5H7: energetics and elastic properties. J Alloy Compd 353(1–2):74–85. doi:10.1016/s0925-8388(02)01324-5

Hector L Jr, Herbst J, Wolf W, Saxe P, Kresse G (2007) Ab Initio thermodynamic and elastic properties of alkaline-earth metals and their hydrides. Phys Rev B 76(1):014121

Heyd J, Scuseria GE, Ernzerhof M (2003) Hybrid functionals based on a Coulomb potential. J Chem Phys 118:8207

Heyd J, Scuseria GE, Ernzerhof M (2006) Erratum:"Hybrid functionals based on a screened Coulomb potential"[J. Chem. Phys. 118, 8207 (2003)]. J Chem Phys 124:219906

Ishikawa A, Okano T, Sugiyama J (1997) Fine structure and tensile properties of ramie fibres in the crystalline form of cellulose I, II, IIII and IVI. Polymer 38(2):463–468. doi:10.1016/S0032-3861(96)00516-2

Jones RM (1975) Mechanics of composite materials, vol 2. Taylor & Francis, London

Kohn W, Sham LJ (1965) Self-consistent equations including exchange and correlation effects. Phys Rev 140(4A):A1133

Kresse G, Furthmuller J (1996a) Efficiency of ab initio total energy calculations for metals and semiconductors using a plane-wave basis set. Comput Mater Sci 6(1):15–50. doi:10.1016/0927-0256(96)00008-0

Kresse G, Furthmuller J (1996b) Efficient iterative schemes for ab initio total-energy calculations using a plane-wave basis set. Phys Rev B 54(16):11169–11186

Kresse G, Hafner J (1994) Ab initio molecular-dynamics simulation of the liquid-metal–amorphous-semiconductor transition in germanium. Phys Rev B 49(20):14251–14269

Lahiji RF, Xu X, , Reifenberger R, Raman A, Rudie A, Moon RJ (2010) Atomic force microscopy characterization of cellulose nanocrystals. Langmuir, 26(6): 4480–4488

Langan P, Sukumar N, Nishiyama Y, Chanzy H (2005) Synchrotron X-ray structures of cellulose Iβ and regenerated cellulose II at ambient temperature and 100 K. Cellulose 12(6):551–562. doi:10.1007/s10570-005-9006-3

Le Page Y, Saxe P (2002) Symmetry-general least-squares extraction of elastic data for strained materials from ab initio calculations of stress. Phys Rev B 65(10):104104

Leslie WC (1981) The physical metallurgy of steels. Hemisphere Publishing Corporation

Li Y, Lin M, Davenport JW (2011) Ab Initio studies of cellulose I: crystal structure, intermolecular forces, and interactions with water. J Phys Chem C 115(23):11533–11539. doi:10.1021/jp2006759

Matsuo M, Sawatari C, Iwai Y, Ozaki F (1990) Effect of orientation distribution and crystallinity on the measurement by X-ray diffraction of the crystal lattice moduli of cellulose I and II. Macromolecules 23(13):3266–3275. doi:10.1021/ma00215a012

Matthews JF, Beckham GT, Bergenstråhle-Wohlert M, Brady JW, Himmel ME, Crowley MF (2012) Comparison of cellulose Iβ simulations with three carbohydrate force fields. J Chem Theory Comput 8(2):735–748. doi:10.1021/ct2007692

Moon RJ, Martini A, Nairn J, Simonsen J, Youngblood J (2011) Cellulose nanomaterials review: structure, properties and nanocomposites. Chem Soc Rev 40(7):3941–3994

Nakamura KI, Wada M, Kuga S, Okano T (2004) Poisson's ratio of cellulose Iβ and cellulose II. J Polym Sci Part B Polym Phys 42(7):1206–1211. doi:10.1002/polb.10771

Nishino T, Takano K, Nakamae K (1995) Elastic modulus of the crystalline regions of cellulose polymorphs. J Polym Sci Part B Polym Phys 33(11):1647–1651. doi:10.1002/polb.1995.090331110

Nishiyama Y, Langan P, Chanzy H (2002) Crystal structure and hydrogen-bonding system in cellulose Iβ from synchrotron X-ray and neutron fiber diffraction. J Am Chem Soc 124(31):9074–9082. doi:10.1021/ja0257319

Nishiyama Y, Sugiyama J, Chanzy H, Langan P (2003) Crystal structure and hydrogen bonding system in cellulose Iα from synchrotron X-ray and neutron fiber diffraction. J Am Chem Soc 125(47):14300–14306. doi:10.1021/ja037055w

Nishiyama Y, Johnson GP, French AD, Forsyth VT, Langan P (2008) Neutron crystallography, molecular dynamics, and quantum mechanics studies of the nature of hydrogen bonding in cellulose Iβ. Biomacromolecules 9(11):3133–3140. doi:10.1021/bm800726v

Nishiyama Y, Langan P, Wada M, Forsyth VT (2010) Looking at hydrogen bonds in cellulose. Acta Crystallogr Sect D 66(11):1172–1177. doi:10.1107/S0907444910032397

Pakzad A, Simonsen J, Heiden PA, Yassar RS (2012) Size effects on the nanomechanical properties of cellulose I nanocrystals. J Mater Res 27(3):528–536

Parthasarathi R, Bellesia G, Chundawat SPS, Dale BE, Langan P, Gnanakaran S (2011) Insights into hydrogen bonding and stacking interactions in cellulose. J Phys Chem A 115(49):14191–14202. doi:10.1021/jp203620x

Perdew JP, Burke K, Ernzerhof M (1996) Generalized gradient approximation made simple. Phys Rev Lett 77(18):3865–3868

Qi Y, Hector LG Jr (2004) Adhesion and adhesive transfer at aluminum/diamond interfaces: a first-principles study. Phys Rev B 69(23):235401

Qi Y, Hector LG (2007) Planar stacking effect on elastic stability of hexagonal boron nitride. Appl Phys Lett 90(8):081922–081923

Qi Y, Guo H, Hector LG, Timmons A (2010) Threefold increase in the Young's modulus of graphite negative electrode during lithium intercalation. J Electrochem Soc 157(5):A558–A566

Roberts R, Rowe R, York P (1994) The Poisson's ratio of microcrystalline cellulose. Int J Pharm 105(2):177–180

Sakurada I, Nukushina Y, Ito T (1962) Experimental determination of the elastic modulus of crystalline regions in oriented polymers. J Polym Sci 57(165):651–660. doi:10.1002/pol.1962.1205716551

Sakurada I, Ito T, Nakamae K (1964) Elastic moduli of polymer crystals for the chain axial direction. Die Makromolekulare Chem 75(1):1–10. doi:10.1002/macp.1964.020750101

Santiago Cintrón M, Johnson G, French A (2011) Young's modulus calculations for cellulose Iβ by MM3 and quantum mechanics. Cellulose 18(3):505–516. doi:10.1007/s10570-011-9507-1

Shang S, Hector L Jr, Wang Y, Zhang H, Liu Z (2009) First-principles study of elastic and phonon properties of the heavy fermion compound CeMg. J Phys: Condens Matter 21(24):246001

Shang S-L, Hector LG Jr, Shi S, Qi Y, Wang Y, Liu Z-K (2012) Lattice dynamics, thermodynamics and elastic properties of monoclinic Li2CO3 from density functional theory. Acta Mater 60(13–14):5204–5216. doi:10.1016/j.actamat.2012.06.006

Šturcová A, His I, Apperley DC, Sugiyama J, Jarvis MC (2004) Structural details of crystalline cellulose from higher plants. Biomacromolecules 5(4):1333–1339

Sugiyama J, Vuong R, Chanzy H (1991) Electron diffraction study on the two crystalline phases occurring in native cellulose from an algal cell wall. Macromolecules 24(14):4168–4175. doi:10.1021/ma00014a033

Tashiro K, Kobayashi M (1991) Theoretical evaluation of three-dimensional elastic constants of native and regenerated celluloses: role of hydrogen bonds. Polymer 32(8):1516–1526. doi:10.1016/0032-3861(91)90435-L

Wada M (2002) Lateral thermal expansion of cellulose Iβ and IIII polymorphs. J Polym Sci Part B Polym Phys 40(11):1095–1102. doi:10.1002/polb.10166

Wada M, Nishiyama Y, Chanzy H, Forsyth T, Langan P (2008) The structure of celluloses. Powder Diffr 23(2):92–95

Wagner R, Moon R, Pratt J, Shaw G, Raman A (2011) Uncertainty quantification in nanomechanical measurements using the atomic force microscope. Nanotechnology 22(45):455703

Woodward C, Trinkle D, Hector L Jr, Olmsted D (2008) Prediction of dislocation cores in aluminum from density functional theory. Phys Rev Lett 100(4):045507

Wróbel J, Hector L Jr, Wolf W, Shang S, Liu Z, Kurzydłowski K (2012) Thermodynamic and mechanical properties of lanthanum–magnesium phases from density functional theory. J Alloy Compd 512(1):296–310

Wu X, Moon R, Martini A (2013) Crystalline cellulose elastic modulus predicted by atomistic models of uniform deformation and nanoscale indentation. Cellulose 20(1):43–55. doi:10.1007/s10570-012-9823-0

Zuluaga MG, Dri FL, Moon RJ, Zavattieri PD (2013a) Anisotropy calculator—3D visualization toolkit. https://nanohub.org/tools/matrix2surface

Zuluaga MG, Dri FL, Moon RJ, Zavattieri PD (2013b) Crystalline cellulose—atomistic toolkit. https://nanohub.org/tools/ccamt